Materials Science in Semiconductor Processing 167 (2023) 107792

Contents lists available at ScienceDirect

Materials Science in Semiconductor Processing

journal homepage: www.elsevier.com/locate/mssp

Full length article

Multiscale atomistic modelling of CVD: From gas-phase reactions to lattice defects

Domenica Raciti [a], Gaetano Calogero [b,*], Damiano Ricciarelli [b], Ruggero Anzalone [a], Giuseppe Morale [a], Domenico Murabito [a], Ioannis Deretzis [b], Giuseppe Fisicaro [b], Antonino La Magna [b,*]

[a] STMicroelectronics, Stradale Primosole, 50, Catania, 95121, Italy
[b] National Research Council, Institute for Microelectronics and Microsystems (IMM-CNR), VIII Strada 5, Catania, 95121, Italy

ARTICLE INFO

Dataset link: https://github.com/MulSKIPS/

Keywords:
CVD
Silicon
Microelectronics
Kinetic-Monte-Carlo
Atomistic

ABSTRACT

Growth from vapour/gas/plasma phases is a key process to produce high-quality nanostructures and thin films. The quest for high performances at low cost calls for the development of modelling strategies able to accurately predict growth rates and structure morphology under a variety of process conditions. In the semiconductor nanotechnology, Lattice Kinetic Monte Carlo (LKMC) is considered an advanced approach for simulating selective epitaxy of semiconductors by Chemical Vapor Deposition (CVD). However, state-of-the-art LKMC tools often neglect fundamental aspects such as lattice defects and chemical reactions, both in the vapor phase and around the evolving surface. We present a multiscale workflow for modelling CVD growth and etching processes also accounting for these critical phenomena. We implement it in the open-source KMC super-Lattice (KMCsL) code MulSKIPS , whose peculiar design allows for the generation and evolution of point-like and extended defects in tetrahedrally-bonded materials, such as Si, SiC or SiGe alloys. Gas-phase reactions at the meso-scale are considered by coupling with an external thermodynamic simulator, while surface reactions involving the equilibrium gas species are described by an analytical continuum model. We perform experiments to calibrate and validate the KMCsL model. We then apply the methodology to simulate nanoscale morphology modifications in planar, nanostructured and constrained geometries, unveiling the role of temperature, precursors' pressures, surface coverage and defects kinetics in the CVD process.

1. Introduction

Growth of nano-structures from vapour/gas/plasma phases is the method of choice to produce high-quality zero, one, two and three dimensional (0D,1D,2D,3D) systems which can eventually have an epitaxial character with respect to the supporting substrate. The demand for increasing performances of nano-fabrication at contained costs motivates the design of modelling strategies able to accurately predict growth rates and structure morphology. In the semiconductor nano-device technology field, Lattice Kinetic Monte Carlo (LKMC) modelling is considered an advanced approach for simulating Si, SiGe, and Ge selective epitaxy by Chemical Vapor Deposition (CVD) and it has also been implemented within state-of-the-art technology computer aided design (TCAD) process models, like Sentaurus Process of Synopsys (https://www.synopsys.com/silicon/tcad/process-simulation/sentaurus-process.html).

The main advantage of LKMC approaches, that makes them suited for multi-scale processes like CVD, is the possibility to simulate time and space scales much wider than ab-initio methods, with atomistic details not accessible from continuum approaches [1]. These features will allow the achievement of a complete process simulation, bridging machine and reactors scales to atomistic properties. For instance, Ref. [2] proposes a LKMC technique for reproducing epitaxial growth of silicon using H_2/SiH_4 chemistry, considering the surface mechanisms of precursor adsorption, surface dissociation higher-order hydrides and hydrogen desorption. Similar approaches [3,4] have been recently developed for several materials/processes, including two-dimensional (2D) materials [5–7] where the 2D atomic distribution further improves the efficiency of the feature scale simulations.

A delicate point concerns the multi-step nature of epitaxial processes, characterized by multiple chemical reactions occurring in the vapour phase and at the solid-vapour phase boundary [8–10], which must be considered for reliable simulations. A systematic approach to gas-phase and interface reactions during epitaxial processes was

* Corresponding authors.
E-mail addresses: gaetano.calogero@imm.cnr.it (G. Calogero), antonino.lamagna@imm.cnr.it (A. La Magna).

https://doi.org/10.1016/j.mssp.2023.107792
Received 3 July 2023; Received in revised form 2 August 2023; Accepted 3 August 2023
Available online 19 August 2023
1369-8001/© 2023 The Authors. Published by Elsevier Ltd. This is an open access article under the CC BY-NC-ND license (http://creativecommons.org/licenses/by-nc-nd/4.0/).

followed, for instance, by Danielsson et al. [11]. Indeed, such reactions have a strong impact on the growth kinetics as well as on the final morphology of the grown material. This consideration holds even for a fixed precursor chemistry, as the final products will vary both from the initial composition (in terms of partial pressures) and from the initial temperature. To this regard, for instance, the distinction between low-temperature and high-temperature regimes is well documented [4,9,12].

In addition to the accurate surface kinetics and related morphology evolution, a super-lattice formulation could add predictive power to the KMC simulations allowing the prediction of internal structural configuration of the growing systems. These features are particularly relevant for the synthesis of nano-structures where atomic configurations are dominated by the tetrahedral bonding character, since they can present cubic, hexagonal or mixed crystal symmetries depending on the process conditions. We notice that the symmetry control of the atomic arrangement in nano-systems is of paramount importance for their application in the fields of electronic, photonic and quantum technologies. A KMC approach on super-Lattice (KMCsL) implementing chemical reactions at the solid-vapour phase boundary for this class of materials has not been developed; and with this study we aim to fill this gap.

In this article we propose a method to simulate with atomic resolution the kinetics of CVD growth processes for group IV compound semiconductors and in general materials with tetrahedral bonding, such as (pristine or doped) Si, Ge or $Si_{1-x}Ge_x$. The method relies on an extension of the MulSKIPS Kinetic Monte Carlo super-Lattice code (https://github.com/mulskips), previously employed for Physical Vapor Deposition (PVD) and Laser Annealing (LA) processes [13–15]. Distinctive features of epitaxial processes, namely the presence of coverage species adsorbed to the evolving surface, as well as chemical reactivity in the bulk gas phase and at the gas-solid interface, are reproduced through a proper definition of the Monte Carlo particles and of the corresponding event probabilities, calibrated against experiments. We apply the method to a chamber with a gaseous mixture of H_2, HCl and SiH_2Cl_2 as an example.

2. Material and methods

2.1. Experiments

Si (0 0 1) epitaxial layers were grown on 200-mm Si wafers from a H_2 + HCl + SiH_2Cl_2 gas mixture in an industrial single-wafer reactor, operating with rotating sample. The total pressure in the chamber was kept constant at 7999 Pa; the precursor pressures ranged from 7788 to 7970 Pa for H_2, from 0 to 155 Pa for HCl and from 30 to 57 Pa for SiH_2Cl_2. The run times t_{run} ensured a grown thickness Δz of the epitaxial layers around 1–10 μm within the investigated temperature ranges (from 1173 K to 1323 K). Thicknesses were measured via a Fourier transform infrared (FTIR) tool, the values Δz being averaged over 9 points per wafer. The growth rates (GR) were finally calculated as $\Delta z/t_{run}$.

2.2. Theory

2.2.1. The KMCsL model

The KMCsL model adopted in this work is based on the assumption that growth (etching) occurs at the interface between the crystal and gas phases as a result of a balance between atom-by-atom transitions from one phase to the other. The system evolution is driven by three types of active KMC particles, defined at the solid-gas interface. These particles, also schematically reported in Fig. 1 along with the associated KMC events, are

(a) "crystal ad-atoms": occupied undercoordinated sites (i.e., with 1 to 3 nearest neighbours) with semiconductor atoms (like Si, Ge or B);
(b) "coverage ad-atoms": occupied undercoordinated sites with non-semiconductor species (such as H or Cl), derived from the precursor molecules;
(c) "ad-voids": empty super-lattice sites which are connected to an ad-atom by one of its dangling bonds

In addition to the active KMC particles, the MulSKIPS code allows the introduction of "wall sites" (Fig. 1d), to define non-evolving regions in the simulation box, such as the substrate or any other geometrical constraint for the evolving surface. An active KMC particle can undergo four possible events during a CVD growth (etching) simulation:

1. "attachment" of a crystal-type atom from the gas phase to an ad-void;
2. "detachment" of a crystal ad-atom, which turns from the solid to the gaseous phase;
3. "adsorption" of a coverage-type atom to an ad-void;
4. "desorption" of a coverage ad-atom, which returns to the gas phase.

The introduction of ad-coverage species and of adsorption/desorption events represents the main difference with respect to the KMCsL implementation for PVD processes [14] (see Supplementary Information for further details).

Importantly, the KMCsL formalism implemented in the MulSKIPS code is able to model the regular lattice of the ideal crystal as a sub-lattice of a cubic super-lattice [13]. This allows to locally reconstruct point-like and extended defective configurations, as they emerge from the reconfiguration of atom positions and bonding in the super-lattice, without labelling the substrate lattice points, under the assumption of a symmetric tetrahedral bonding configuration. Two tetrahedral bonding configurations are allowed in the KMC super-lattice, namely that of cubic (zinc-blend) or hexagonal (wurtzite) crystal phases. Whenever a deposition event occurs on a site S with coordination number $n = 1$, its bonding configuration with potential neighbours is set to either cubic or hexagonal, depending on the surrounding environment. If the bonding configurations of its next-neighbours are mostly set to cubic (hexagonal), then the stacking choice made for the S site will be cubic (hexagonal). Instead, if the bonding configurations of its next-neighbours are equally distributed between cubic and hexagonal, then there is a user-defined probability Ptranszig to initiate a new phase. Setting Ptranszig=1 leads to the ideal defect-free crystal structure. Importantly, reciprocity is always imposed when choosing the bonding configuration, i.e., a bond can form only if two nearest-neighbour sites point the relative orbitals in the same direction.

Notice that, since only atomic species are eligible as active KMC particles, molecular species and their reactivity cannot be described explicitly. Molecular fluxes and chemical reactions occurring in the gas phase and at the evolving crystal-gas interface are therefore translated into fluxes of individual atomic species reaching the surface and undergoing single-atom phase transitions.

2.2.2. KMCsL calibration strategy

The KMC events described in the previous section are selected stochastically according to predefined event rates, whose parameters are carefully calibrated to account for all possible chemical phenomena occurring during the CVD process, within a given precursor environment and under given thermodynamic conditions. A proper calibration strategy is crucial to couple the reactor-scale features of the process to the atomic scale of KMC transition probabilities and material morphology. We followed a stepwise approach (summed up in Fig. 2):

1. Collection of an experimental database for planar Si growth (etching) from the chosen precursors at varying pressures and temperatures;
2. Calculation, for each experiment, of the gas-phase equilibrium composition;

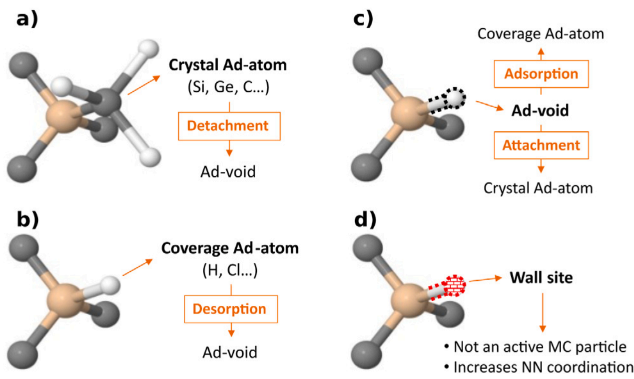

Fig. 1. Particle types implemented in the MulSKIPS KMCsL framework. The kinetic events eligible for each particle are indicated, along with the resulting particle states. (a) Crystal ad-atoms are active KMC particles which can only undergo detachment events, turning into ad-voids. (b) Coverage adatoms can only undergo desorption events, turning into ad-voids. (c) Ad-voids can undergo either attachment events, turning into crystal ad-atoms, or adsorption events, turning into coverage ad-atoms. (d) Wall sites are inactive KMC particles. Their position is fixed for the whole duration of the simulation and their role is to increase by one the coordination of all nearest crystal or coverage ad-atoms.

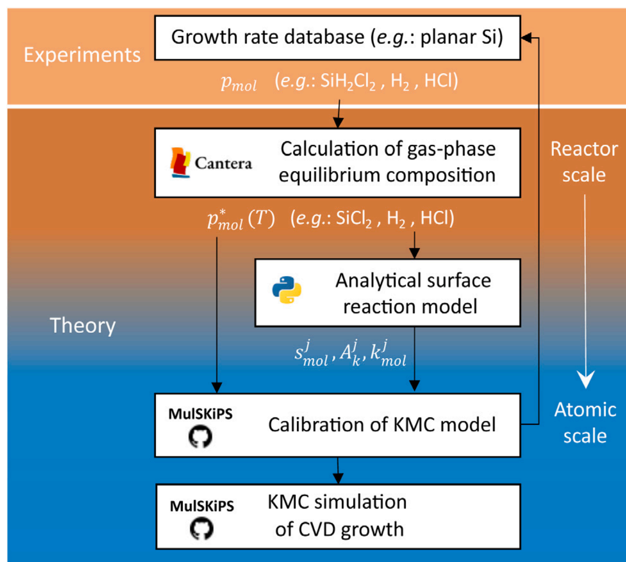

Fig. 2. Schematics of the calibration procedure, detailed in the main text, enabling the translation of the reactor-scale features (temperature and precursor pressures p_{mol}) into KMC event rates that can be used to predict the growth (etching) kinetics with atomistic detail.

3. Definition and calibration of an analytical model for growth (etching), based on the surface reactions of the equilibrium gas species;
4. Definition and calibration of the KMCsL event rates, building on the calibrated analytical model;
5. KMCsL simulation of a specific CVD process and geometry.

The so-calibrated KMCsL model can be used to simulate different process conditions and/or substrate geometries involving the chosen precursors' chemistry. We note that other state-of-the-art KMC-based CVD simulators are usually calibrated without taking into account step 2. In this study we considered H_2 + HCl + SiH_2Cl_2 as a case study, but the approach can be generalized to different precursors with system-specific adjustments (see 2.2.4). See the Supporting Information for further technical details.

2.2.3. Calculation of gas-phase equilibrium composition

The first calibration step consists in the steady-state calculation of chemical reactions in the gas phase. This allows, given the chosen experimental conditions (precursor species, pressure and temperature), to identify the gas species that are more likely to interact with the evolving surface. At this stage we neglect thermo-fluid dynamics transport in the reactor. This aspect, which is relevant especially for confined geometries, may be included in a future development of the code by appropriately coupling to external mass transport tools. To implement gas-phase homogeneous reactions in our code, we took advantage of the open-source software Cantera [16], imported in a dedicated Python routine following the provided documentation. All the species potentially involved in gas-phase equilibria for the chosen precursor chemistry and all the corresponding reactions were embedded in a customized database. For each species, the database reports the element composition and the 7-Coefficient NASA polynomial parameterization for various temperature ranges (from 300 to 5000 K) [17], which are used to calculate its thermodynamic properties (molar heat capacity at constant pressure, molar enthalpy, and absolute molar entropy). For each reaction, the stoichiometry, reaction order and Arrhenius parameters (pre-factor and energy barrier) are reported, distinguishing between forward and backward reactions. These parameters are used by Cantera to calculate the rate constant k of each reaction (backward and forward) and, consequently, the molar fractions χ^* of product species, as a function of the molar fractions χ of the reactants and of the process temperature T.

An example of our calculation output for the H_2 + HCl + SiH_2Cl_2 case study is provided in Fig. 3a. The calculations were set up with an initial mixture of H_2 (7813 Pa), HCl (155 Pa) and SiH_2Cl_2 (31 Pa) and involved 24 chemical species and 40 chemical reactions, among the hundreds listed in the database. For temperatures above 1200 K, the main species in the gas phase at equilibrium are found to be H_2, HCl and $SiCl_2$. Hence, under these thermodynamic conditions, the latter three species should be considered as those actually reaching the surface and contributing to its local evolution.

2.2.4. Analytical model of surface reactions

Based on the results of gas-phase equilibrium calculations, we wrote a 0D analytical model of growth of a flat Si substrate, accounting for the attachment/detachment of the obtained molecular species, i.e., $SiCl_2$, HCl and H_2. The following simplified reaction sequence was used:

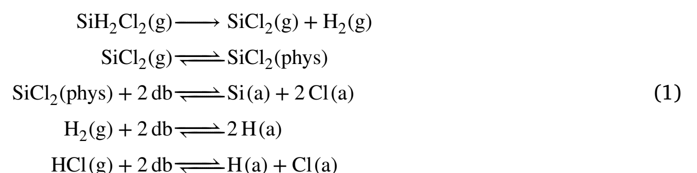

$$\begin{aligned} SiH_2Cl_2(g) &\longrightarrow SiCl_2(g) + H_2(g) \\ SiCl_2(g) &\rightleftharpoons SiCl_2(phys) \\ SiCl_2(phys) + 2\,db &\rightleftharpoons Si(a) + 2\,Cl(a) \\ H_2(g) + 2\,db &\rightleftharpoons 2\,H(a) \\ HCl(g) + 2\,db &\rightleftharpoons H(a) + Cl(a) \end{aligned} \tag{1}$$

where g stands for bulk gas phase; phys=physisorbed state, a =adsorbate, db=dangling bond; double-headed arrows indicate reversible reactions, single-headed arrows denote irreversible reactions. Assuming a precursor-mediated adsorption/desorption mechanisms [18,19] for $SiCl_2$, HCl and H_2, reactions Eq. (1) lead to the following system of coupled differential equations in the surface coverages Θ_i, with $i = \mathrm{H, Cl, Si}$ (see Ref. [20]), where SiH_2Cl_2 is assumed instead of $SiCl_2$:

$$\frac{d\Theta_H}{dt} = 2s_{H_2}F^*_{H_2} + s_{HCl}F^*_{HCl} - 2k_{H_2}\Theta_H^2 + - k_{HCl}\Theta_{Cl}\Theta_H \tag{2}$$

$$\frac{d\Theta_{Cl}}{dt} = 2s_{SiCl_2}F^*_{SiCl_2} + s_{HCl}F^*_{HCl} - 2k_{SiCl_2}\Theta_{Cl}^2 + - k_{HCl}\Theta_{Cl}\Theta_H \tag{3}$$

$$\frac{d\Theta_{Si}}{dt} = s_{SiCl_2}F^*_{SiCl_2} - k_{SiCl_2}\Theta_{Cl}^2 \tag{4}$$

Here, $F^*_{mol} = \frac{p^*_{mol}}{\sqrt{2\pi M_{mol}RT}}$ is the impingement flux of the precursor species mol (mol = $SiCl_2$, HCl, H_2; stars referring to the gas-phase equilibrium

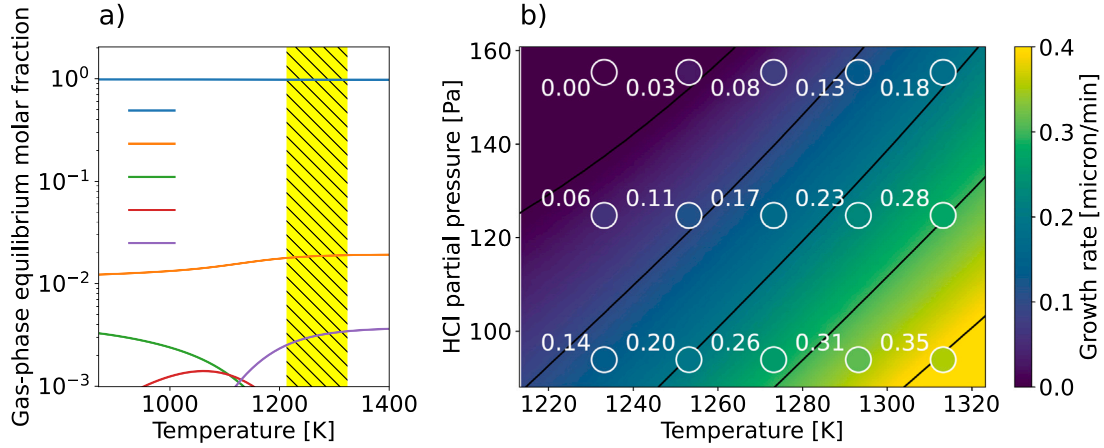

Fig. 3. (a) Example of gas-phase steady-state calculation results. Mole fractions of reaction products as a function of temperature, obtained from an initial mixture of H_2 (7813 Pa), HCl (155 Pa) and SiH_2Cl_2 (31 Pa). Only the species above a molar fraction threshold of 10^{-3} are displayed. In the temperature range of all the experiments considered in this work (yellow area), the mixture components are H_2, HCl and $SiCl_2$. (b) Growth rate obtained from the analytical model of surface reactions while fixing the above recipe, but varying the HCl partial pressure p_{HCl}. Contour lines correspond to the ticks' values in the colorbar. The circles represent growth rates measured at p_{HCl}=155 Pa, 125 Pa and 94 Pa. The analytical model reasonably reproduces the expected trend of increasing growth rate with decreasing p_{HCl}, as well as their expected temperature dependence.

values in the mixture, obtained from Cantera outputs, with partial pressures $p^*_{\mathrm{mol}} = p_{\mathrm{tot}}\chi^*_{\mathrm{mol}}$); $k_{\mathrm{mol}} = A_{\mathrm{mol}}e^{-\epsilon_{\mathrm{mol}}/\mathrm{k_B}T}$ is a kinetic desorption constant; s_{mol} is the so-called reactive sticking coefficient of mol, whose simplest form is [18,21]:

$$s_{\mathrm{mol}} = s^0_{\mathrm{mol}}\frac{\Theta^{\mathrm{free}}_{\mathrm{db}}}{\Theta^{\mathrm{tot}}_{\mathrm{db}}} \tag{5}$$

with $\Theta^{\mathrm{tot}}_{\mathrm{db}}$ being the surface density of dangling bonds for the chosen orientation of the crystal substrate ($\sim 6.3 \cdot 10^{18}$ m^{-2} for Si(1 0 0)), $\Theta^{\mathrm{free}}_{\mathrm{db}}$ the surface density of the ones available for adsorption and s^0_{mol} the initial sticking coefficient, which can be written as [20–23]:

$$s^0_{\mathrm{mol}} = \frac{\alpha_{\mathrm{mol}}}{1 + \beta_{\mathrm{mol}}\exp\left[-\epsilon_{\mathrm{mol}}/RT\right]} \tag{6}$$

where α_{mol}, β_{mol} and ϵ_{mol} are precursor-dependent parameters, assumed to remain constant over the whole temperature range.

Concerning surface coverage, the saturation values (and hence $\Theta^{\mathrm{free}}_{\mathrm{db}}$ in Eq. (5)) depend in principle on both the species i (e.g., H vs Cl) and the precursor for a given species (e.g., HCl vs Cl_2 or SiH_2Cl_2) [20,22,24,25]. As a first approximation, we assume that both H and Cl saturate the surface upon formation of a monolayer, regardless of the precursor, and that the total coverage saturates at $\Theta_{\mathrm{sat}} = \Theta^{\mathrm{tot}}_{\mathrm{db}}$:

$$\Theta_{\mathrm{sat}} = \Theta^{\mathrm{tot}}_{\mathrm{db}} = \Theta_{\mathrm{Cl}} + \Theta_{\mathrm{H}} + \Theta^{\mathrm{free}}_{\mathrm{db}} \tag{7}$$

A steady-state equilibrium condition is assumed with conditions $\frac{d\Theta_{\mathrm{H}}}{dt} = 0$ (Eq. (2)) and $\frac{d\Theta_{\mathrm{Cl}}}{dt} = 0$ (Eq. (3)). Coverage concentrations for hydrogen and chlorine satisfy the following set of algebraic equations:

$$\begin{aligned} 2\mathrm{k}_{\mathrm{SiCl_2}}\Theta^2_{\mathrm{Cl}} + \mathrm{k}_{\mathrm{HCl}}\Theta_{\mathrm{H}}\Theta_{\mathrm{Cl}} &= \left(2\mathrm{s}_{\mathrm{SiCl_2}}\mathrm{F}^*_{\mathrm{SiCl_2}} + \mathrm{s}_{\mathrm{HCl}}\mathrm{F}^*_{\mathrm{HCl}}\right) \\ 2\mathrm{k}_{\mathrm{H_2}}\Theta^2_{\mathrm{H}} + \mathrm{k}_{\mathrm{HCl}}\Theta_{\mathrm{H}}\Theta_{\mathrm{Cl}} &= \left(2\mathrm{s}_{\mathrm{H_2}}\mathrm{F}^*_{\mathrm{H_2}} + \mathrm{s}_{\mathrm{HCl}}\mathrm{F}^*_{\mathrm{HCl}}\right) \end{aligned} \tag{8}$$

According to this model, the Si growth rate GR can be calculated by solving the system Eq. (8), substituting Θ_{H} and Θ_{Cl} into Eq. (4) and dividing by the Si atomic density, $\rho^{at}_{Si} = 5.02 \times 10^{28}$ m^{-3}:

$$\mathrm{GR} = \frac{d\Theta_{\mathrm{Si}}}{dt}/\rho^{at}_{Si} \tag{9}$$

Fig. 3b shows the growth rate calculated from the analytical model of surface reactions while fixing a partial pressure of 7813 Pa for H_2 and 31 Pa for SiH2Cl$_2$, respectively, and varying the HCl partial pressure p_{HCl}. Growth rates measured at p_{HCl} = 155 Pa, 125 Pa and 94 Pa are also plotted for comparison. The analytical model reasonably reproduces the expected trend of increasing growth rate with decreasing HCl pressure, as well as their expected temperature dependence. Slight deviations (below 0.5 μm/min) are only found for low HCl pressure at the highest considered temperatures.

Importantly, when simulating different process conditions where different gas species (other than $SiCl_2$, HCl and H_2) are present in the equilibrium gas mixture, the current model must be corrected to account for those species (and the corresponding model parameters must be calibrated accordingly).

2.2.5. Definition of KMCsL event rates

The outputs of gas-phase calculations and of the surface reactions analytical model provided a starting point for the KMCsL model calibration. The frequencies of the KMC events described in Section 2.2.1 were defined as follows:

(i) Attachment probability:

$$\nu^i_{\mathrm{att}}(n) = B_0\sum_{\mathrm{mol}} c^i_{\mathrm{mol}}\frac{p^*_{\mathrm{mol}}}{\sqrt{2\pi \mathrm{M_{mol}}\mathrm{R}T}}s_{\mathrm{mol}} \tag{10}$$

(ii) Detachment probability:

$$\nu^i_{\mathrm{det}}(n) = B_0 \cdot B_1\Theta^2_{\mathrm{sat}} \cdot e^{E_{\mathrm{det}}(n)/\mathrm{k_B}T}\sum_{\mathrm{mol}} c^i_{\mathrm{mol}}A_{\mathrm{mol}}e^{-\epsilon_{\mathrm{mol}}/\mathrm{k_B}T} \tag{11}$$

(iii) Adsorption probability:

$$\nu^j_{\mathrm{ads}}(n) = B_0\sum_{\mathrm{mol}} c^j_{\mathrm{mol}}\frac{p^*_{\mathrm{mol}}}{\sqrt{2\pi \mathrm{M_{mol}}\mathrm{R}T}}s_{\mathrm{mol}} \tag{12}$$

(iv) Desorption probability:

$$\nu^j_{\mathrm{des}}(n) = B_0 \cdot B_1\Theta^2_{\mathrm{sat}}\sum_{\mathrm{mol}} c^j_{\mathrm{mol}}A_{\mathrm{mol}}e^{-\epsilon_{\mathrm{mol}}/\mathrm{k_B}T} \tag{13}$$

where n is the coordination number of the crystal ad-atom involved in the transition; mol are the major gas-phase species at equilibrium, with molar mass M_{mol} and partial pressure p^*_{mol}; $c^{i(j)}_{\mathrm{mol}}$ is the stoichiometric coefficient of species $i(j)$ in molecule mol, superscripts i and j denoting crystal and coverage species, respectively; s_{mol} is the sticking coefficient, as appearing in Eqs. (2)–(4); A_{mol} and ϵ_{mol} are the prefactors and energy barriers of the desorption coefficients k_{mol}; the term $B_1\Theta^2_{\mathrm{sat}}$, with B_1 being a constant, multiplied by the sum on the right side of Eqs. (11) and (13) has units of a desorption rate as in Eqs. (2)–(4); $B_0 \sim \Theta^{-1}_{\mathrm{sat}}$ ensures overall units of a frequency; $\mathrm{k_B}T$ and R are the Boltzmann and gas constants and T the process temperature; $E_{\mathrm{det}}(n)$ is a coordination-dependent detachment barrier.

Most of the above parameters are fixed by calibrating the analytical model against the measured temperature-dependent growth rate. The only parameters specific to the KMCsL model are B_0, B_1 and $E_{det}(n)$. The latter corresponds to a matrix of coordination-dependent detachment probabilities which, in the simplest case, do not distinguish between different neighbour species, reducing to 3 values only, $E_{det}(1)$, $E_{det}(2)$ and $E_{det}(3)$. In this work, to keep the number of calibration parameters as low as possible, we introduce only one exception to this simplified framework in the cases where the local neighbour configuration would favour desorption of the crystal species in a stable molecular form. Since Si atoms in our model can only detach from the surface in the form of $SiCl_2$ molecule (see Eq. (4)), we indeed set $E_{det}(n) \equiv E_{det}(2) - \Delta E$ (with $\Delta E > 0$) for all Si atoms ending up with 2 Cl neighbours during the simulation, with ΔE being an additional calibration parameter.

We remark that the full matrix of KMCsL probabilities (not only the detachment ones) can in principle be defined to depend on neighbour chemical environment (e.g., chemical type and bonding coordination). This increases significantly the number of potential knobs to turn, but it makes this CVD framework readily applicable to other crystal-precursors combinations.

3. Results and discussion

3.1. KMCsL simulations of Si(0 0 1) CVD growth

Fig. 4 shows the results of step 3 and 4 of the calibration workflow described in Section 2.2.2 for a CVD growth of Si along the (0 0 1) direction (equivalent to z in the KMCsL coordinate system). We used a total pressure of 7999 Pa and p_{H_2}=7813 Pa, p_{HCl}=155 Pa and $p_{SiH_2Cl_2}$=31 Pa (the same mixture as in Fig. 3a), in a temperature range where the dominant gas species are represented by H_2, HCl and $SiCl_2$. The values used in the analytical model (found at step 3 of the workflow) and those of the 6 additional KMCsL-specific parameters are reported in Table 1. The coverages Θ_H and Θ_{Cl} as a function of temperature are shown in Fig. 4a, along with the overall surface coverage (Θ_H+Θ_{Cl}). These curves reflect a clear tendency to desorb H and Cl species as temperature increases, and higher Cl coverage compared to H. Remarkably, these results demonstrate that, despite the significant intrinsic differences between analytical and KMCsL approaches, the two models provide quite similar results if calibrated using the proposed workflow. A reasonably good agreement between the two models can also be observed when comparing the growth rates obtained as a function of temperature. This is shown in Fig. 4b, where the experimental data used as reference for the calibration are also reported. Fig. 4 also demonstrates a strong correlation between the trends of growth rate and surface coverages as a function of temperature. The growth is indeed slower at lower temperatures, where a larger saturation of surface dangling bonds by coverage species occurs and where a higher ratio between Cl and H coverages favours detachment events in the form of $SiCl_2$. Both the analytical and the KMCsL model predict a negative growth rate in the temperature range where no growth was measurable (below ~1260 K). This can be attributed to Cl-mediated surface etching, which is modelled in our simulations but could not be carefully assessed in the experiment due to the negligible variation in measured layer thickness. Compared to the analytical model, the KMCsL predicts a quite lower etching velocity. We note that such agreement with experimental measurements was achieved using a temperature-independent set of calibration parameters. In principle, different sets of parameters could be used for different temperature regimes when needed.

3.2. KMCsL simulations of CVD growth with stacking defects

The advanced KMCsL CVD simulations presented hereafter were obtained by considering a temperature T=1263 K, where the gas-phase equilibrium calculation yields H_2, HCl and $SiCl_2$ as dominant molecular species, with p_{H_2}=7820 Pa, p_{HCl}=148 Pa and p_{SiCl_2}=25 Pa.

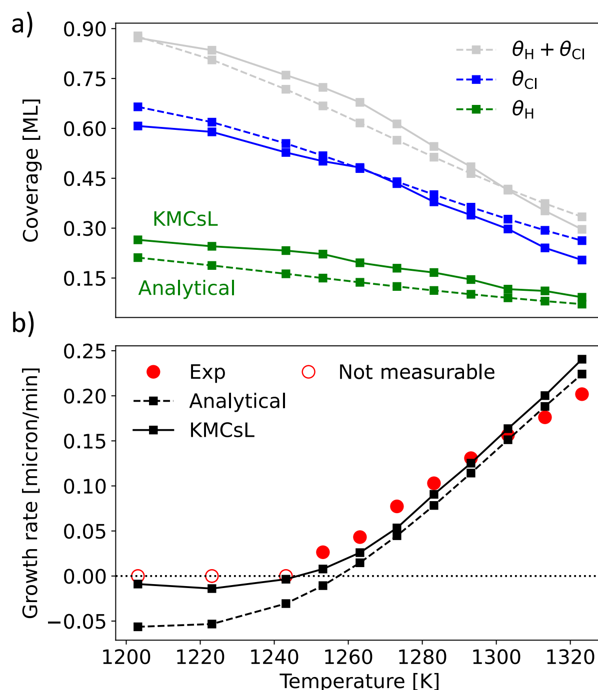

Fig. 4. Results of the workflow for a CVD growth of Si(0 0 1). (a) H (green) and Cl (blue) coverages and total (grey) surface coverage predicted by the analytical model (dashed lines) and the KMCsL model (solid lines). (b) Growth rate as a function of temperature predicted by the KMCsL model (black solid line), compared to the experimental data (red circles) and to the predictions of the analytical model (black dashed line). Empty red circles indicate temperatures at which grown thickness could not be measured.

Table 1
Calibration parameters used in the analytical and KMCsL models for Si(0 0 1) CVD growth simulation.

	H_2	$SiCl_2$	HCl
A [m²/s]	$2.4 \cdot 10^{-4}$	$8.4 \cdot 10^{-6}$	$6.6 \cdot 10^{-3}$
ε [eV]	2.69	2.91	3.12
α	$9.7 \cdot 10^{21}$	$2.6 \cdot 10^{23}$	$2.7 \cdot 10^{22}$
β	$1.2 \cdot 10^{9}$	$6 \cdot 10^{2}$	$8.4 \cdot 10^{6}$
ϵ [eV]	1.57	0.165	1.6
KMCsL specific parameters			
B_0 [m²]		$1.6 \cdot 10^{-19}$	
B_1		0.1	
$E_{det}(1)$ [eV]		−0.4	
$E_{det}(2)$ [eV]		0.3	
$E_{det}(3)$ [eV]		1.11	
ΔE [eV]		0.5	

In this section we show that the atomistic framework presented so far can be applied to simulate defective CVD growth. We consider a model of a Si(0 0 1) surface, represented via a KMCsL cell of $21 \times 21 \times 43$ nm³, periodic along x and y (see Fig. 5a). In order to maximize the probability of forming stacking defects, we structure the initial surface as a 2D array of inverted pyramids with faces along the {< 1 1 1 >} directions. The latter only expose sites with n = 1, which are those allowed to trigger polymorphic transitions from cubic to hexagonal crystal phases and viceversa (see Section 2.2.1). Fig. 5b shows the final state of the solid-gas interface in a simulation of ~26 s with a $P_{TRANSZIG}$=0.95. A self-closing triple stacking fault is generated during the growth, with the typical hexagonally stacked crystal layer highlighted in purple. Vacancies are also formed during the process simulation, shown in red, representing empty sites that get surrounded by filled sites with n < 4 during the simulation. We note that their density in an actual CVD process might be lower, due to their possible diffusion towards the surface (not implemented in

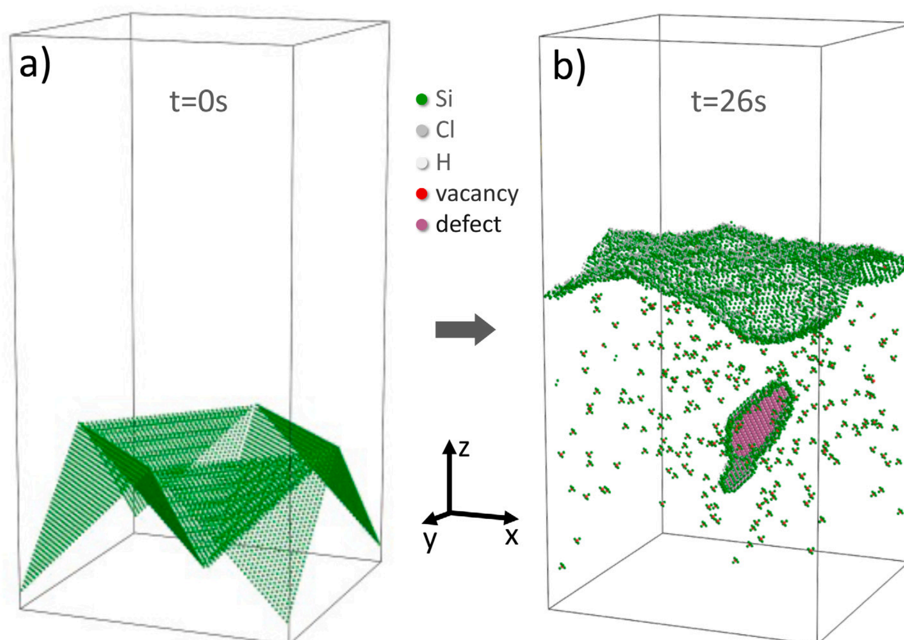

Fig. 5. KMCsL simulation of CVD growth from a Si inverted pyramid substrate, obtained by imposing p_{H_2}=7813 Pa, p_{HCl}=155 Pa, $p_{SiH_2Cl_2}$=31 Pa, T=1263 K and allowing for defect formation (PTRANSZIG=0.95). (a) Input substrate geometry made of {1 1 1} Si surfaces. (b) System evolution after a 26 s simulated growth, with formation of a triple stacking fault defect. Undercoordinated Si atoms in the default cubic stacking are shown in green; H atoms in white; Cl atoms in gray; vacancies in red. Hexagonally stacked Si atoms are superposed to the cubic ones and represented as purple spheres.

the current model). Such diffusion could slightly affect growth/etching rates and bulk defectivity, requiring further calibration adjustments, but it is not expected to impact on surface morphology, governed by the balance among the coordination-dependent event rates. We also note that, in principle, PTRANSZIG could be analytically expressed as a function of relevant physical quantities, such as temperature, and calibrated against ad-hoc bulk defectivity measurements.

3.3. KMCsL simulations of nanoparticle CVD growth

In this section we show that the atomistic framework can also be applied to simulate clean or defective CVD growth of nano-objects evolving in three dimensions. We consider an initially spherical Si nanocrystal with 7 nm diameter (Fig. 6a) and carry out a CVD growth simulation of 36 s, which yields the expected reshaping into an energetically more favourable, {1 1 1}-faceted octahedral nanoparticle (Fig. 6b), often observed experimentally [26]. The same simulation carried out with PTRANSZIG=0.9 (Fig. 6c) gives rise to a roughly octahedral nanoparticle with several stacking defects, in the form of triple stacking faults or local hexagonal crystalline domains. The morphology and phase composition of the nanoparticle in actual experiments can be approximately reproduced by proper tuning of PTRANSZIG during calibration.

3.4. KMCsL simulations of constrained CVD growth

The CVD KMCsL simulation can also be initiated from a TCAD input geometry. Non-evolving regions in the KMCsL box can be modelled as clusters of wall sites (see Section 2.2.1). For example, in Fig. 7 we consider an initial $5 \times 5 \times 3$ nm^3 Si nanocrystal (blue in Fig. 7a) lying on a non-evolving substrate and laterally constrained by a vertical non-evolving region (red in Fig. 7a). The latter could represent, for instance, the insulating substrate and the gate stack in a fully-depleted silicon-on-insulator (FDSOI) device. The initial solid-gas interface in the KMCsL box at t=0, initializing the growth, is therefore a 3D roughly cubic nucleus (green in Fig. 7a). A clean CVD growth simulation yields the expected emergence of {1 1 1} faces (Fig. 7b). The same simulation carried out with PTRANSZIG=0.99 gives rise to a roughly similar behaviour, but with several stacking defects and quite large hexagonal crystalline domains (Fig. 7c). PTRANSZIG can be further tuned to achieve predictions in closer agreement with measured morphology and polymorphisms.

3.5. Applicability of the CVD KMCsL framework

The current CVD implementation in MulSKIPS allows up to 3 crystal species and 3 coverage species in the growth (etching) simulation. This is enough to reproduce typical precursor recipes of CVD processes for the most relevant elemental and binary semiconductors with tetrahedral bonding (SiGe, SiC, GaN, GaAs, InP etc.), including dopant species (without diffusion or activation kinetics). The main requirement is the availability of a suitable set of experimental data and the appropriate calibration of kinetic parameters. More species may be added in future developments of the code. An example of KMCsL simulation of CVD growth of 30 nm $Si_{1-x}Ge_x$:B layer on a Si(0 0 1) substrate, with emergence of a triple stacking fault, is reported in Fig. 8. The purpose of this simulation is only to demonstrate the extension capabilities of the developed atomistic CVD framework. An ad-hoc KMCsL parameter set was indeed designed without the use of CANTERA or benchmarks with experimental results, in order to reproduce the CVD growth of a layer with 30% Ge content and a B concentration of $\sim 2.3 \cdot 10^{20}$ cm^{-3}.

4. Conclusions

The methodology presented in this work contains the key elements for the accurate predictions of the nano-structural evolution during a CVD process, namely: the calculation of macroscopic variables at the reactor scale, the interface model to estimate the effective atomic impingement rate at the vapour-solid surface from the precursors' fluxes, the super lattice formulation of the atomistic feature scale model to simulate the relationship between morphology and internal structures of the growing nano-system. We notice that the Kinetic Monte Carlo method is mandatory for the latter simulation due to the long-time of the CVD process, with its super lattice solution being essential to

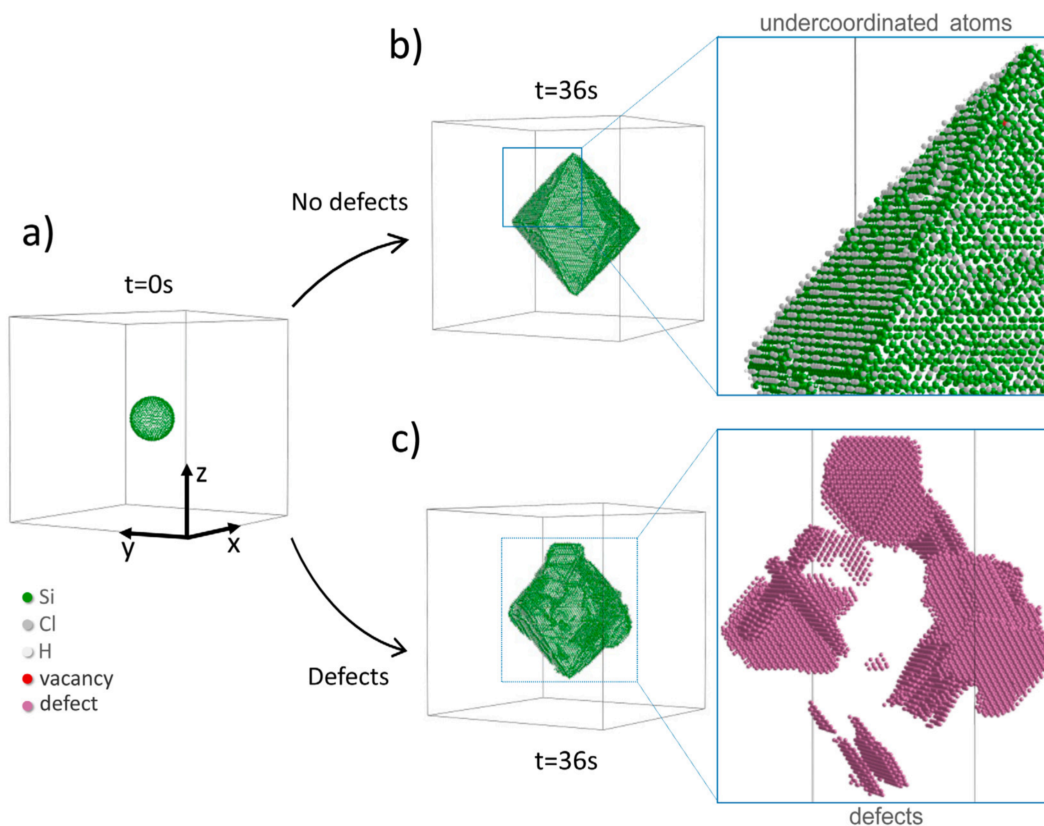

Fig. 6. KMCsL simulation of CVD growth of a Si spherical nanoparticle, obtained by imposing p_{H_2}=7813 Pa, p_{HCl}=155 Pa, $p_{SiH_2Cl_2}$=31 Pa, T=1263 K. (a) Initial solid-gas interface. (b) Crystal morphology after a 36 s simulated growth in the absence of defects (PTRANSZIG=1) and (c) allowing for their formation (PTRANSZIG=0.9). Undercoordinated cubic Si atoms are shown in green; H atoms in white; Cl atoms in gray; vacancies in red; hexagonally stacked atoms in purple.

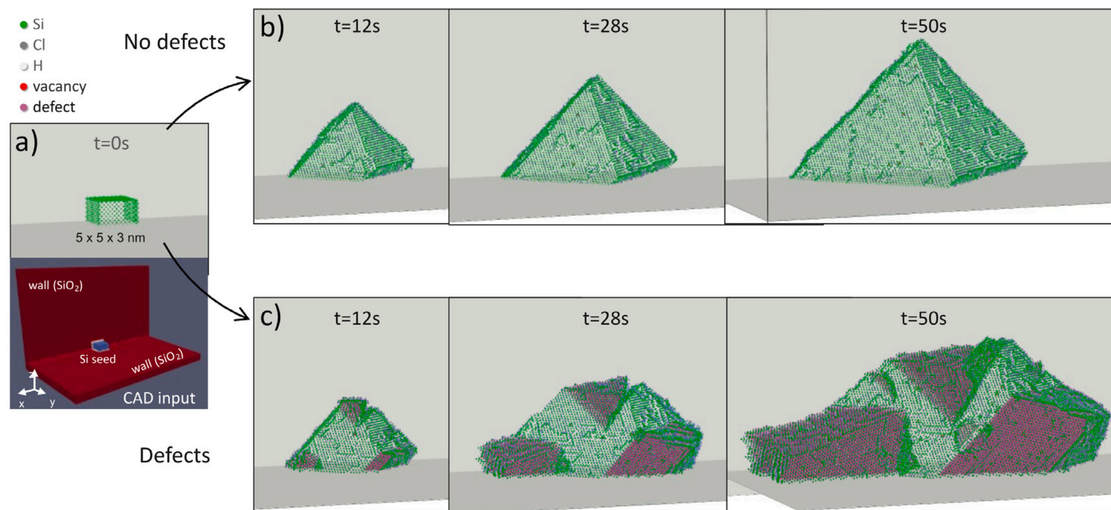

Fig. 7. KMCsL simulation of CVD growth of a Si nanocrystal confined between two walls, obtained by imposing p_{H_2}=7813 Pa, p_{HCl}=155 Pa, $p_{SiH_2Cl_2}$=31 Pa, T=1263 K. (a) Input KMCsL substrate geometry (nucleus surface in green) and associated TCAD structure (nucleus in blue and walls in red). (b) Crystal morphology evolution during the growth in the absence of defects (PTRANSZIG=1) and (c) in their presence (PTRANSZIG=0.99). Undercoordinated cubic Si atoms are shown in green; H atoms in white; Cl atoms in gray; vacancies in red; hexagonally stacked atoms in purple.

include stacking disorder often observed experimentally. Partial advancements in this fully multiscale approach have been considered in the past literature in the field, but the implementation of the complete approach for the CVD process, and in particular the final coupling with a KMC super lattice scheme dedicated to the CVD case with disorder, has not been considered so far. Notably, the full computational workflow is implemented in a completely open-source process simulation tool, i.e., MULSKIPS . The particular process' examples discussed here are representative of the application of the multiscale scheme to the advanced technological design of real processes. The parameter calibration has been assessed and validated with the aid of an experimental Desing of Experiments (DoE) in blanket samples, where the model/experiment comparisons are facilitated, for specific machine settings (for additional examples see Calogero et al. [27]). Then, the simulation potential is demonstrated for nano-constrained

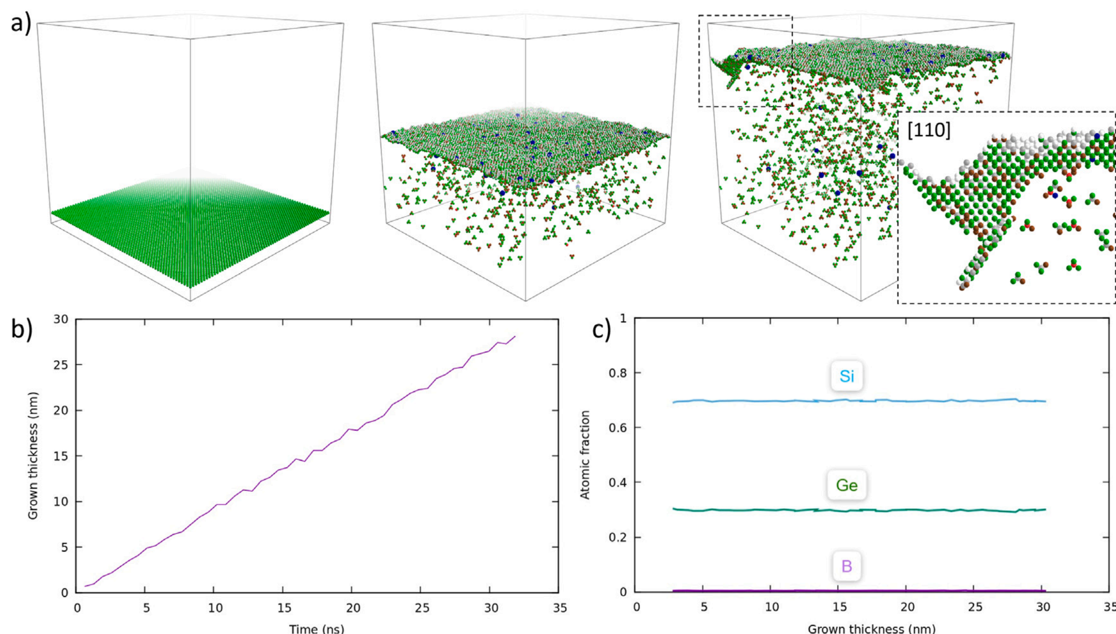

Fig. 8. KMCsL simulation of CVD growth of 30 nm $Si_{1-x}Ge_x$:B layer on a Si(0 0 1) substrate. An ad-hoc calibration was chosen, only for demonstration purposes, such to reproduce the growth of a layer with 30% Ge content and a B concentration of $\sim 2.3 \cdot 10^{20}$ cm^{-3} (without a full calibration workflow). (a) Snapshots of surface morphology during the growth. The [1 1 0] view in the inset shows a small stacking defect emerging during the simulation (PTRANSZIG=0.95). Si, Ge, B, H and Cl undercoordinated atoms are represented in green, brown, blue, white and gray, respectively, while vacancies are in red. (b) Layer thickness over time. (c) Fraction of species in the layer as a function of layer thickness.

systems for the realization of Virtual Design of Experiments (V-DoE), which can complement and integrate with minimal cost the real DoE in a large and complex set of conditions. This application scheme can be potentially replicated for different applications, beyond the precursors' chemistry and thermodynamic parameters here spanned, maintaining the same accuracy level to guarantee the proper adherence to the machine dependent setting and the possibility of real micro-structural predictions.

CRediT authorship contribution statement

Domenica Raciti: Conceptualization, Investigation, Visualization, Validation, Formal analysis, Methodology, Data curation, Writing – original draft. **Gaetano Calogero:** Conceptualization, Investigation, Visualization, Validation, Formal analysis, Methodology, Data curation, Writing – original draft. **Damiano Ricciarelli:** Investigation, Data curation, Writing – review & editing. **Ruggero Anzalone:** Investigation, Data curation. **Giuseppe Morale:** Investigation, Data curation. **Domenico Murabito:** Investigation, Data curation. **Ioannis Deretzis:** Investigation, Data curation, Writing – review & editing. **Giuseppe Fisicaro:** Investigation, Data curation, Methodology, Visualization, Validation, Writing – review & editing. **Antonino La Magna:** Investigation, Methodology, Conceptualization, Formal analysis, Funding acquisition, Project administration, Software, Supervision, Writing – original draft.

Declaration of competing interest

The authors declare that they have no known competing financial interests or personal relationships that could have appeared to influence the work reported in this paper.

Data availability

The minimal input data needed to replicate the findings reported in the article is available, in the form of python notebooks, on GITHUB and can be accessed here: https://github.com/MulSKIPS/.

Acknowledgements

We gratefully acknowledge funding from the European Union's Horizon 2020 Research and Innovation programme under grant agreement No. 871813 MUNDFAB.

Appendix A. Code availability

The methodology presented in this work is implemented in the open-source tool MulSKIPS available on GITHUB and can be accessed via this link: https://github.com/MulSKIPS.

Appendix B. Supplementary material

Supplementary material related to this article can be found online at https://doi.org/10.1016/j.mssp.2023.107792.

References

[1] C.C. Battaile, D.J. Srolovitz, Kinetic monte carlo simulation of chemical vapor deposition, Annu. Rev. Mater. Res. 32 (2002) 297–319, http://dx.doi.org/10.1146/annurev.matsci.32.012102.110247.

[2] J.P. Balbuena, I. Martin-Bragado, Lattice Kinetic Monte Carlo simulation of epitaxial growth of silicon thin films in H_2/SiH_4 chemical vapor deposition systems, Thin Solid Films 634 (2017) 121–133.

[3] N. Cheimarios, D. To, G. Kokkoris, G. Memos, A.G. Boudouvis, Monte Carlo and Kinetic Monte Carlo models for deposition processes: a review of recent works, Front. Phys. 9 (2021b) 631918.

[4] N. Cheimarios, G. Kokkoris, A. Boudouvis, Multiscale modeling in chemical vapor deposition processes: models and methodologies, Arch. Comput. Methods Eng. 28 (2021a) 637–672.

[5] P. Li, Z. Li, J. Yang, Dominant kinetic pathways of graphene growth in chemical vapor deposition: The role of hydrogen, J. Phys. Chem. C 121 (2017) 25949–25955, http://dx.doi.org/10.1021/acs.jpcc.7b09622.

[6] K. Momeni, Y. Ji, Y. Wang, S. Paul, S. Neshani, D.E. Yilmaz, Y.K. Shin, D. Zhang, J.W. Jiang, H.S. Park, S. Sinnott, A. van Duin, V. Crespi, L.Q. Chen, Multiscale computational understanding and growth of 2d materials: a review, npj Comput. Mater. 6 (2020) http://dx.doi.org/10.1038/s41524-020-0280-2.

[7] A. Govind Rajan, J.H. Warner, D. Blankschtein, M.S. Strano, Generalized mechanistic model for the chemical vapor deposition of 2d transition metal dichalcogenide monolayers, ACS Nano 10 (2016) 4330–4344, http://dx.doi.org/10.1021/acsnano.5b07916, pMID: 26937889.

[8] J.M. Jasinski, S.M. Gates, Silicon chemical vapor deposition one step at a time: fundamental studies of silicon hydride chemistry, Accounts Chem. Res. 24 (1991) 9–15.

[9] K. Choy, Chemical vapour deposition of coatings, Prog. Mater. Sci. 48 (2003) 57–170.

[10] L. Sun, G. Yuan, L. Gao, J. Yang, M. Chhowalla, M.H. Gharahcheshmeh, K.K. Gleason, Y.S. Choi, B.H. Hong, Z. Liu, Chemical vapour deposition, Nat. Rev. Methods Primers 1 (2021) 1–20.

[11] O. Danielsson, M. Karlsson, P. Sukkaew, H. Pedersen, L. Ojamae, A systematic method for predictive in silico chemical vapor deposition, J. Phys. Chem. C 124 (2020) 7725–7736.

[12] J. Jasinski, B. Meyerson, B. Scott, Mechanistic studies of chemical vapor deposition, Ann. Rev. Phys. Chem. 38 (1987) 109–140.

[13] A. La Magna, A. Alberti, E. Barbagiovanni, C. Bongiorno, M. Cascio, I. Deretzis, F. La Via, E. Smecca, Simulation of the growth kinetics in group IV compound semiconductors, Phys. Status Solidi (a) 216 (2019) 1800597.

[14] G. Fisicaro, C. Bongiorno, I. Deretzis, F. Giannazzo, F. La Via, F. Roccaforte, M. Zielinski, M. Zimbone, A. La Magna, Genesis and evolution of extended defects: The role of evolving interface instabilities in cubic SiC, Appl. Phys. Rev. 7 (2020) 021402.

[15] G. Calogero, D. Raciti, P. Acosta-Alba, F. Cristiano, I. Deretzis, G. Fisicaro, K. Huet, S. Kerdilès, A. Sciuto, A. La Magna, Multiscale modeling of ultrafast melting phenomena, npj Comput. Mater. 8 (2022) 1–10.

[16] D.G. Goodwin, H.K. Moffat, I. Schoegl, R.L. Speth, B.W. Weber, Cantera: An object-oriented software toolkit for chemical kinetics, thermodynamics, and transport processes, 2022, http://dx.doi.org/10.5281/zenodo.6387882, https://www.cantera.org, version 2.6.0.

[17] B.J. McBride, NASA Glenn Coefficients for Calculating Thermodynamic Properties of Individual Species, National Aeronautics and Space Administration, John H. Glenn Research Center ..., 2002.

[18] W. Weinberg, M. Grunze, H. Kreuzer, Kinetics of interface reactions, in: Springer Series in Surface Science, Vol. 8, 1987, pp. 94–125.

[19] D.J. Doren, J.C. Tully, Precursor-mediated adsorption and desorption: a theoretical analysis, Langmuir 4 (1988) 256–268.

[20] P. Coon, M. Wise, S. George, Modeling silicon epitaxial growth with SiH_2Cl_2, J. Cryst. Growth 130 (1993) 162–172.

[21] D.A. King, M. Wells, Reaction mechanism in chemisorption kinetics: nitrogen on the {100} plane of tungsten, Proc. R. Soc. Lond. Ser. A Math. Phys. Eng. Sci. 339 (1974) 245–269.

[22] P. Coon, P. Gupta, M.L. Wise, S. George, Adsorption and desorption kinetics for SiH_2Cl_2 on Si (111) 7 × 7, J. Vacuum Sci. Technol. A 10 (1992) 324–333.

[23] H. Rauscher, The interaction of silanes with silicon single crystal surfaces: microscopic processes and structures, Surf. Sci. Rep. 42 (2001) 207–328.

[24] M. Liehr, C. Greenlief, M. Offenberg, S. Kasi, Equilibrium surface hydrogen coverage during silicon epitaxy using SiH_4, J. Vacuum Sci. Technol. A 8 (1990) 2960–2964.

[25] Gao Q., C. Cheng, P. Chen, W. Choyke, J. Yates Jr., Comparison of Cl_2 and HCl adsorption on Si (100)-(2 × 1), Thin Solid Films 225 (1993) 140–144.

[26] G. Mannino, A. Alberti, R. Ruggeri, S. Libertino, A.R. Pennisi, G. Faraci, Octahedral faceted si nanoparticles as optical traps with enormous yield amplification, Sci. Rep. 5 (2015) http://dx.doi.org/10.1038/srep08354.

[27] G. Calogero, I. Deretzis, G. Fisicaro, M. Kollmus, F. La Via, S.F. Lombardo, M. Scholer, P.J. Wellmann, A. La Magna, Multiscale simulations for defect-controlled processing of group IV materials, Crystals (ISSN: 2073-4352) 12 (12) (2022) 1701, http://dx.doi.org/10.3390/cryst12121701, https://www.mdpi.com/2073-4352/12/12/1701.